

STEVE – Space-Time-Enclosing Volume Extraction

B. R. Schlei

Abstract—The novel STEVE (*i.e.*, Space-Time-Enclosing Volume Extraction) algorithm is described here for the very first time. It generates iso-valued hypersurfaces that may be implicitly contained in four-dimensional (4D) data sets, such as temporal sequences of three-dimensional images from time-varying computed tomography. Any final hypersurface that will be generated by STEVE is guaranteed to be free from accidental rifts, *i.e.*, it always fully encloses a region in the 4D space under consideration. Furthermore, the information of the interior/exterior of the enclosed regions is propagated to each one of the tetrahedrons, which are embedded into 4D and which in their union represent the final, iso-valued hypersurface(s). STEVE is usually executed in a purely data-driven mode, and it uses lesser computational resources than other techniques that also generate simplex-based manifolds of codimension 1.



1 INTRODUCTION

THE following presentation is subject to a pending patent application (*cf.*, Ref. [1]).

Recent advances in the field of computed tomography (*cf.*, e.g., Ref.s [2]– [4]) have made available high-quality 4D¹ reconstructed sets of measured time-varying voxel data. Similarly structured data may be generated while simulating 4D transversal phase-spaces in ion beam transport, or in 3 + 1D fireball simulations in the field of theoretical heavy-ion physics, just to name a few more examples (*cf.*, section 4). Given such *discrete* 4D data, its further processing may require the extraction or generation of a certain number of *continuous*, iso-valued hypersurfaces that may or may not be contained in the data.

Quite a number of papers deal with the subject of iso-(hyper)surface construction in higher dimensions already (*cf.*, e.g., Ref.s [5]– [11]). Their approaches are usually based on methods that can be used also for contour and surface extraction in two dimensions (2D) and 3D, respectively. E.g., in Ref.s [6], [7], the 4D data are extruded to the fifth dimension (5D) while representing them as a set of 4-simplices². Iso-hypersurfaces are then constructed while intersecting the 4-simplices at a constant level in 5D. However, this technique does not ensure the construction of manifolds of codimension 1.

Analogously, Weigle and Banks' method would represent a 2D gray-level image as a triangular surface relief in 3D. In order to construct 1D contours, the relief would be intersected with a 2D plane at fixed iso-value. However, since relief triangles could be oriented parallel to and totally coincide with the intersecting plane, the resulting object would not just simply consist of line segments, but – perhaps – also of triangles. Note that in this paper we are especially concerned with the generation of simplex-based manifolds of codimension 1, *i.e.*, hypersurfaces that *purely* consist of 3-simplices (tetrahedrons), which are embedded

into the considered 4D spaces.

The latter requirement is fulfilled by the work of other authors, where some of these algorithms could be categorized as follows: those algorithms, which (i) use templates (*cf.*, e.g., Ref.s [8], [9]), or (ii) construct a mesh via (oriented) edge insertion, and which implicitly solve ambiguities (*cf.*, Ref. [11]³), or (iii) are *protomesh*-based, and which solve spatial and temporal ambiguities explicitly (this present work; *cf.*, Ref. [10] for a first announcement).

This paper is organized as follows. First we shall shortly revisit VESTA [12], *i.e.*, an algorithm that generates iso-surfaces in 3D from volumetric (e.g., image) data. Next, we shall present a common flowchart for the various processing stages of both VESTA and STEVE, because both algorithms work in a very similar way. While presenting the volume extraction framework, we are going to introduce the indexing scheme used by STEVE for the 4D spaces under consideration, as well as a complete, corresponding vector path table (*cf.*, Table 2). This table will provide all possible and/or necessary links for volume segments that contribute to the final hypersurfaces.

Special emphasis will be put onto the consistent treatment of topological ambiguities. In particular, we shall demonstrate that in *discretized* 4D spaces *more than one* solution is generally possible for the constructed iso-hypersurfaces. In an application related section, we provide a few examples for hypersurface extraction. And last but not least, we discuss STEVE in comparison to other 4D hypersurface generation algorithms. This paper will conclude with a short summary.

2 THREE DIMENSIONS

The marching variant of VESTA [12] treats each individual $2 \times 2 \times 2$ -neighborhood of a 3D (e.g., image) data set separately. In Fig. 1, we show the indexing scheme that VESTA uses for each 3D-cell, together with the 3D coordinate system, $x|y|z$, as indicated in Fig. 1.d. Each neighborhood cube has six faces that are each represented by the junctures (gray

• B. R. Schlei is with the GSI Helmholtz Centre for Heavy Ion Research GmbH, Planckstraße 1, 64291 Darmstadt, Germany.

1. *I.e.*, three spatial dimensions (3D) and one temporal dimension (+1D).

2. *I.e.*, pentachorons, pentatopes, or tetrahedral hyperpyramids.

3. Another algorithm is provided by the much earlier work of Fidrich [5]

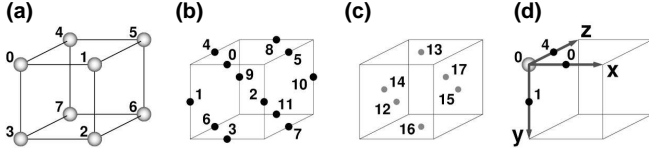


Fig. 1. Indexing scheme for a $2 \times 2 \times 2$ -neighborhood of voxels; (a) voxel site IDs; (b) boundary face centers; (c) junctures; (d) range vectors for voxel no. 0, coinciding with the 3D coordinate system $x|y|z$, and superimposed with corresponding boundary face centers.

dots) as shown in Fig. 1.c. The cubes' twelve edges are represented by the boundary face centers (black dots) as shown in Fig. 1.b, whereas its eight corners are the centers of each voxel of the considered voxel neighborhood (cf., Fig. 1.a). Fig. 1.d also shows the three range vectors of voxel no. 0, along which the final surface support points⁴ may be moved if interpolations are necessary.

In addition to this indexing scheme, VESTA makes use of a vector path table (cf., Table 1), which provides all possible and/or necessary links for surface segments that contribute to the final iso-surfaces. Next, we shall demonstrate the 3D surface construction with VESTA with the example shown in Fig. 2 in conjunction with the flowchart pictured in Fig. 3.

After VESTA has read proper input data (cf., Fig. 3.a), a user-specified iso-value leads to a segmentation, i.e., a classification of the $2 \times 2 \times 2$ -neighborhoods (cf., Fig. 3.b). In Fig. 2, we only the two voxels with the site IDs 0 and 2 have been selected while assuming that they have field values above or equal to a given iso-value (cf., Fig. 2, except Fig. 2.c). In the following, let us call selected voxels "active", and all remaining voxels "inactive".

VESTA introduces for each contact between an active and an inactive voxel a protomesh "building block" (PBB) as indicated in Figs 5.b, 6.b, & 6.c. In Fig. 2.a, these show up as six quadrants, whereas in Fig. 2.b, they are indicated by twelve voxel face vectors (VFFV) and six corresponding boundary face centers (black dots) with the IDs 0, 1, 2, 3, 4,

4. The boundary face centers are support points of the final surfaces (cf., Ref. [12], for more detail).

TABLE 1
Directed paths for the quadrants of the oriented boundary faces

Center ID	\oplus Path	\ominus Path
0	13 \rightarrow 0 \rightarrow 12	12 \rightarrow 0 \rightarrow 13
1	12 \rightarrow 1 \rightarrow 14	14 \rightarrow 1 \rightarrow 12
2	15 \rightarrow 2 \rightarrow 12	12 \rightarrow 2 \rightarrow 15
3	12 \rightarrow 3 \rightarrow 16	16 \rightarrow 3 \rightarrow 12
4	14 \rightarrow 4 \rightarrow 13	13 \rightarrow 4 \rightarrow 14
5	13 \rightarrow 5 \rightarrow 15	15 \rightarrow 5 \rightarrow 13
6	16 \rightarrow 6 \rightarrow 14	14 \rightarrow 6 \rightarrow 16
7	15 \rightarrow 7 \rightarrow 16	16 \rightarrow 7 \rightarrow 15
8	17 \rightarrow 8 \rightarrow 13	13 \rightarrow 8 \rightarrow 17
9	14 \rightarrow 9 \rightarrow 17	17 \rightarrow 9 \rightarrow 14
10	17 \rightarrow 10 \rightarrow 15	15 \rightarrow 10 \rightarrow 17
11	16 \rightarrow 11 \rightarrow 17	17 \rightarrow 11 \rightarrow 16

Note: The quadrants of the oriented boundary faces have their centers at the predefined locations as pictured in Fig. 1.b. The start and end points of the 24 paths are potential points of ambiguity, as shown in Fig. 1.c. For the orientations, cf., Appendix A.

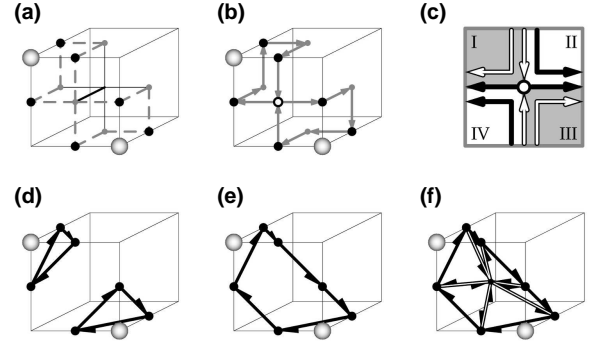


Fig. 2. Encounter of a topological ambiguity within a 3D-cell: (a) initial boundary faces; (b) protomesh; (c) connectivity diagram. (d) two resulting oriented triangles from the "disconnect" mode; (e) a final, more complex-shaped surface segment, resulting from the "connect" mode; (f) as in (e), with a surface segment decomposition into six triangles.

and 7. In addition, Fig. 2.b shows five junctures (gray dots) with IDs 12, 13, 14, 15, and 16. The initial paths (cf., Fig. 3.c) of this cell can be read off from Table 1. These are the paths with no.s (center ID / orientation) $0 \oplus$, $1 \oplus$, $2 \ominus$, $3 \ominus$, $4 \oplus$, and $7 \oplus$.

The juncture with ID 12 is a so-called "point of ambiguity" (POA, cf., Fig. 3.d). Where all other selected junctures feature exactly one incoming and one outgoing VFFV, the POA has two incoming and two outgoing VFFVs. The connectivity diagram as shown in Fig. 2.c helps one to resolve the consistent concatenation of VFFVs (cf., Fig. 3.e). If an incoming VFFV that is part of the PBB of a given voxel will be connected to an outgoing VFFV of another PBB of the *same* voxel, then one operates in the so-called "disconnect" mode. Otherwise, if one connects it to an outgoing VFFV of another PBB of a *different* voxel, then one operates in the so-called "connect" mode.

Either choice of concatenation leads to the formation of a 3D protomesh (cf., Fig. 2.b). In the "disconnect" mode one obtains here the two meshes $13 \rightarrow 0 \rightarrow 12 \rightarrow 1 \rightarrow 14 \rightarrow 4 \rightarrow 13$, and $12 \rightarrow 2 \rightarrow 15 \rightarrow 7 \rightarrow 16 \rightarrow 3 \rightarrow 12$, whereas in the "connect" mode one obtains here the single mesh $13 \rightarrow 0 \rightarrow 12 \rightarrow 2 \rightarrow 15 \rightarrow 7 \rightarrow 16 \rightarrow 3 \rightarrow 12 \rightarrow 1 \rightarrow 14 \rightarrow 4 \rightarrow 13$. After the removal of the junctures (or joints, cf., Fig. 3.f), one is left with polytopes⁵ in 3D (cf., Fig. 3.h).

In the "disconnect" mode one obtains here the two vector cycles $0 \rightarrow 1 \rightarrow 4 \rightarrow 0$, and $2 \rightarrow 7 \rightarrow 3 \rightarrow 2$, as shown in Fig. 2.d, whereas in the "connect" mode one obtains here the single vector cycle $0 \rightarrow 2 \rightarrow 7 \rightarrow 3 \rightarrow 1 \rightarrow 4 \rightarrow 0$, as shown in Fig. 2.e. Hence, in the "disconnect" mode we end up with two oriented triangles (VESTA 3-cycles), and no further processing is necessary. However, in the "connect" mode we end up with one oriented VESTA 6-cycle. In Fig. 2.f, this vector cycle has been decomposed into six oriented triangles (cf., Figs 3.i and 14.6.b). VESTA has stored at this stage the generated 2-simplices (cf., Fig. 3.j) and thereby completes its processing. Note that we did not demonstrate the interpolation of support points (cf., Fig. 3.g) in this example.

5. The constructed polytopes are shaped irregularly in general (cf., Ref. [13]).

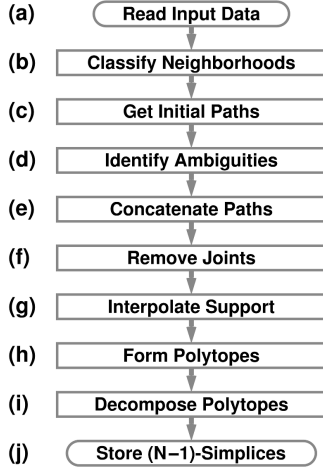


Fig. 3. Flowchart for both VESTA and STEVE (see text).

3 THE VOLUME EXTRACTION FRAMEWORK

Note that because of Ref. [1], we exhibit in this paper neither any source code nor any pseudocode of the STEVE algorithm. However, we present – among many other things – a flowchart that represents its various processing steps (*cf.*, Fig. 3). We shall address each single stage of this flowchart in one or more of the following subsections.

3.1 Initial Mesh Features

The geometrical structure of the underlying meshes (or grids), which support the data that should be processed, is as follows. Here, we shall consider purely homogeneous, N -cubical (cartesian) grids only, with N referring to the integral dimension of the space under consideration. We choose N , because we intend to compare our 4D method with analogue 2D and 3D techniques. In particular, we shall use two different approaches. Either we shall look at the data globally, or we shall look at a $2(\times 2)^{N-1}$ -neighborhood of the data. In the first case we shall use the term “global view” (GV), and in the last case we shall use the term “neighborhood view” (NV), respectively. Furthermore, let

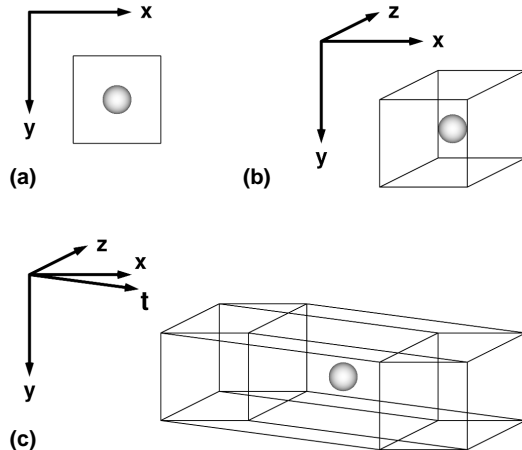


Fig. 4. Coordinate systems in (a) 2D with a single pixel; (b) 3D with a single voxel; and (c) 4D with a single toxel.

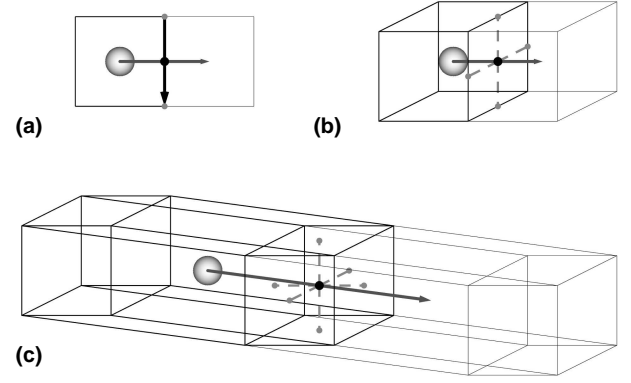


Fig. 5. Pairs of picture elements that are in direct contact in (a) 2D; (b) 3D; and (c) 4D (see text).

the fourth dimension – without loss of generality – be named “time”⁶.

In Fig. 4, various coordinate systems that we are going to use ($x|y$ in 2D, $x|y|z$ in 3D, and $x|y|z|t$ in 4D, respectively) are shown together with samples of single, corresponding picture elements (in GV). The centers of the elements, i.e., a pixel, a voxel, and a toxel (i.e., time-varying voxel) are each marked with a sphere.

The STEVE algorithm starts with the reading of proper input data (*cf.*, Fig. 3.a). This input should specify the overall dimensions of the 4D space under consideration, e.g., by indicating the bounds and maximum numbers of toxels of the homogeneous 4D grid in the $x|y|z|t$ -directions. Furthermore, it should consist of the individual $x|y|z|t$ -positions and one (or more⁷) field value(s) that is (are) associated with each center of the corresponding toxels.

Next, we shall discuss the segmentation of the data, i.e., the differentiation of picture elements (or data cells) that should be enclosed with a manifold of codimension 1 from those that should not be enclosed.

3.2 Data Segmentation

After STEVE has obtained proper input, the specification of an iso-value will allow for the segmentation of these data. I.e., toxels that have a (selected) field value larger than or equal to the iso-value will be marked for enclosure, whereas the others will not, or vice versa. Hence, the segmentation of a 4D space leads to a classification of its various toxel neighborhoods (*cf.*, Fig. 3.b). In Fig. 5, we show – in GV – pairs of picture elements in each 2D, 3D, and 4D that are in direct contact. In each dimension one element is active, i.e., it is marked for enclosure (indicated by the spheres), and the other element is considered inactive, i.e., it should not be enclosed (no spheres are placed in their centers).

In Fig. 5, each center of an active element is the origin of a range vector, which ends in the center of the inactive neighboring picture element. These range vectors (dark gray; *cf.*, Fig. 6) define the bounds within which a support point (black dots) of the final extracted, iso-valued manifolds may be repositioned. E.g., the STEVE algorithm

⁶ Note however, that we do not necessarily consider a metric here.

⁷ This, of course, depends on the particular application one may have in mind.

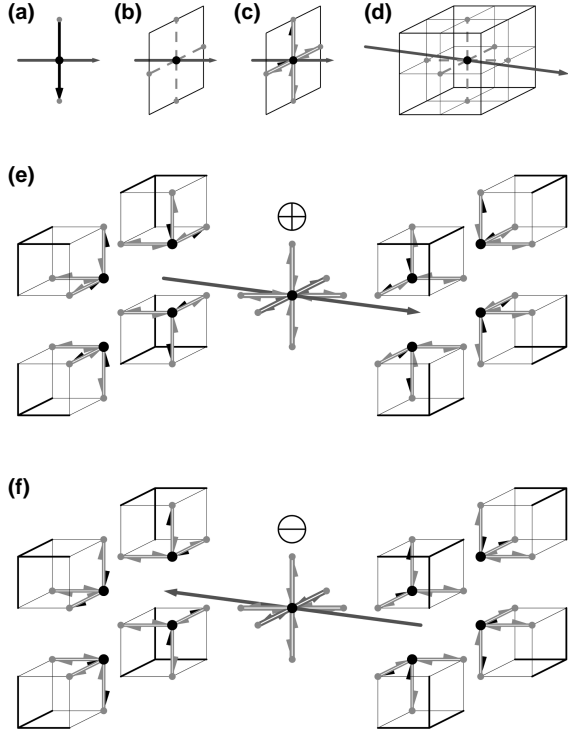


Fig. 6. Initial protomesh building blocks for contour, surface and hyper-surface construction in (a) for 2D, in (b) & (c) for 3D, and in (d) – (f) for 4D, respectively (see text).

uses linear interpolation⁸ for this purpose at some later stage in the processing (*cf.*, Fig. 3.g).

The transitions from an active picture element to an inactive one are of particular interest here. They are shown once again in Fig. 6. For the sake of completeness, Fig. 6.a depicts the building block that allows for contour extraction in 2D with DICONEX (*cf.*, Ref. [16] for more detail). In 3D, VESTA concatenates single squares with the help of VFVs, which have been described in the previous section (*cf.*, Figs 6.b and 6.c). In analogy, STEVE concatenates single cubes in 4D. The new 4D building block, which aids this concatenation, is shown (in GV) in Fig. 6.d (dashed lines⁹); in Fig. 6.e, as exploded view for *positive* orientation (\oplus , i.e., the range vector points into positive x -, y -, z -, or t -direction, respectively); in Fig. 6.f, as exploded view for *negative* orientation (\ominus , i.e., the range vector points into negative x -, y -, z -, or t -direction, respectively).

Note that in Figs 6.e and 6.f, the tiny black arrows mark toxel cube vectors (TCV) pairs, which belong together. All TCV pairs connect a juncture of volumes (i.e., cubes) that are in contact to another volume through a 4D support point (black dots) with another juncture (gray dots).

3.3 Indexing Scheme and Vector Paths

It is sufficient to discuss all transitions from active to inactive toxels within single $2 \times 2 \times 2 \times 2$ -neighborhoods (or 4D-cells).

⁸. More complicated types of interpolations than just simple linear interpolations are possible. E.g., one could use (higher-dimensional) B-Splines [14], [15] instead, etc.

⁹. Dashed lines represent internal vector paths, so-called “toxels cube vectors”.

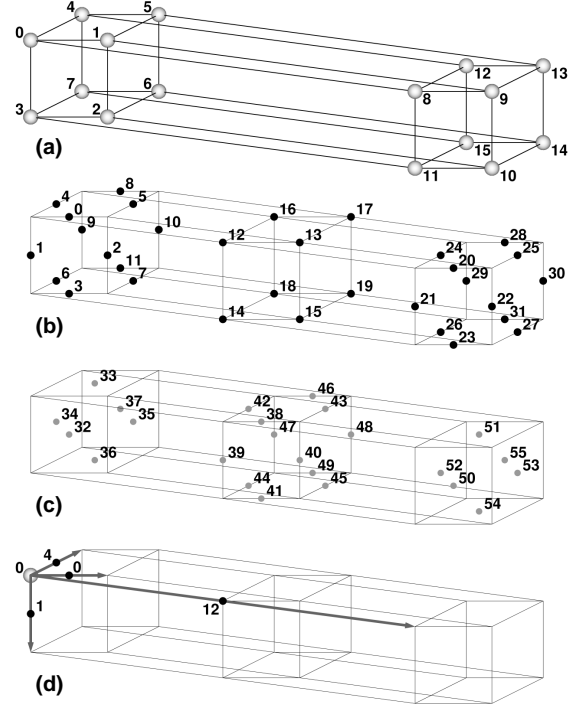


Fig. 7. Indexing scheme for a $2 \times 2 \times 2 \times 2$ -neighborhood of toxels; (a) toxel site IDs; (b) boundary cube centers; (c) junctures; (d) range vectors for toxel no. 0, superimposed with corresponding boundary cube centers.

Therefore, we label each relevant 4D point of a given 4D-cell with a unique index.

In Fig. 7, we show the notations that we have chosen for a given 4D-cell (in NV). In Fig. 7.a, all sixteen toxel site IDs are shown. Since we have named the fourth dimension time (*cf.*, above), let No.s 0 through 7 represent the “past,” and no.s 8 through 15 the “future”. In Fig. 7.b, all thirty-two potential boundary cube centers (i.e., final manifold support points) are pictured. And finally, in Fig. 7.c, all twenty-four junctures – which are potential points of ambiguity (POA) – are shown for neighboring boundary cubes. As an example, Fig. 7.d, shows for toxel no. 0 four range vectors (with positive (i.e., \oplus) orientations each in the x -, y -, z -, and t -directions), superimposed with their corresponding boundary cube centers. Note that the central cubes in Figs 7.b–d represent in this chosen context the “present”.

As Fig. 7.d shows, each of the sixteen toxels may contribute within the 4D-cell with exactly four boundary volume octants (i.e., an eights of a full boundary cube). Note that each boundary volume octant (BVO) is represented within STEVE by a *triplet* of TCV pairs (*cf.*, Figs 6.e and 6.f). Hence, one has in total $16 \times 4 \times 3 = 192$ different possible vector paths (i.e., TCV pairs) within a given toxel neighborhood. The indexing scheme as shown in Fig. 7 and the table of the 192 vector paths (*cf.*, Table 2) form two of the three main ingredients that STEVE uses for iso-hypersurface construction.

The third main ingredient for STEVE is a connectivity diagram (*cf.*, Fig. 18.c) that helps to resolve topological ambiguities, whenever a juncture actually is a POA. The latter will be discussed further down below.

TABLE 2
Triplets of directed paths for the octants of the oriented boundary cubes

Center ID	\oplus Path 1	\oplus Path 2	\oplus Path 3	\ominus Path 1	\ominus Path 2	\ominus Path 3
0	33 \rightarrow 0 \rightarrow 32	32 \rightarrow 0 \rightarrow 38	38 \rightarrow 0 \rightarrow 33	32 \rightarrow 0 \rightarrow 33	33 \rightarrow 0 \rightarrow 38	38 \rightarrow 0 \rightarrow 32
1	32 \rightarrow 1 \rightarrow 34	34 \rightarrow 1 \rightarrow 39	39 \rightarrow 1 \rightarrow 32	34 \rightarrow 1 \rightarrow 32	32 \rightarrow 1 \rightarrow 39	39 \rightarrow 1 \rightarrow 34
2	35 \rightarrow 2 \rightarrow 32	32 \rightarrow 2 \rightarrow 40	40 \rightarrow 2 \rightarrow 35	32 \rightarrow 2 \rightarrow 35	35 \rightarrow 2 \rightarrow 40	40 \rightarrow 2 \rightarrow 32
3	32 \rightarrow 3 \rightarrow 36	36 \rightarrow 3 \rightarrow 41	41 \rightarrow 3 \rightarrow 32	36 \rightarrow 3 \rightarrow 32	32 \rightarrow 3 \rightarrow 41	41 \rightarrow 3 \rightarrow 36
4	34 \rightarrow 4 \rightarrow 33	33 \rightarrow 4 \rightarrow 42	42 \rightarrow 4 \rightarrow 34	33 \rightarrow 4 \rightarrow 34	34 \rightarrow 4 \rightarrow 42	42 \rightarrow 4 \rightarrow 33
5	33 \rightarrow 5 \rightarrow 35	35 \rightarrow 5 \rightarrow 43	43 \rightarrow 5 \rightarrow 33	35 \rightarrow 5 \rightarrow 33	33 \rightarrow 5 \rightarrow 43	43 \rightarrow 5 \rightarrow 35
6	36 \rightarrow 6 \rightarrow 34	34 \rightarrow 6 \rightarrow 44	44 \rightarrow 6 \rightarrow 36	34 \rightarrow 6 \rightarrow 36	36 \rightarrow 6 \rightarrow 44	44 \rightarrow 6 \rightarrow 34
7	35 \rightarrow 7 \rightarrow 36	36 \rightarrow 7 \rightarrow 45	45 \rightarrow 7 \rightarrow 35	36 \rightarrow 7 \rightarrow 35	35 \rightarrow 7 \rightarrow 45	45 \rightarrow 7 \rightarrow 36
8	37 \rightarrow 8 \rightarrow 33	33 \rightarrow 8 \rightarrow 46	46 \rightarrow 8 \rightarrow 37	33 \rightarrow 8 \rightarrow 37	37 \rightarrow 8 \rightarrow 46	46 \rightarrow 8 \rightarrow 33
9	34 \rightarrow 9 \rightarrow 37	37 \rightarrow 9 \rightarrow 47	47 \rightarrow 9 \rightarrow 34	37 \rightarrow 9 \rightarrow 34	34 \rightarrow 9 \rightarrow 47	47 \rightarrow 9 \rightarrow 37
10	37 \rightarrow 10 \rightarrow 35	35 \rightarrow 10 \rightarrow 48	48 \rightarrow 10 \rightarrow 37	35 \rightarrow 10 \rightarrow 37	37 \rightarrow 10 \rightarrow 48	48 \rightarrow 10 \rightarrow 35
11	36 \rightarrow 11 \rightarrow 37	37 \rightarrow 11 \rightarrow 49	49 \rightarrow 11 \rightarrow 36	37 \rightarrow 11 \rightarrow 36	36 \rightarrow 11 \rightarrow 49	49 \rightarrow 11 \rightarrow 37
12	38 \rightarrow 12 \rightarrow 39	39 \rightarrow 12 \rightarrow 42	42 \rightarrow 12 \rightarrow 38	39 \rightarrow 12 \rightarrow 38	38 \rightarrow 12 \rightarrow 42	42 \rightarrow 12 \rightarrow 39
13	40 \rightarrow 13 \rightarrow 38	38 \rightarrow 13 \rightarrow 43	43 \rightarrow 13 \rightarrow 40	38 \rightarrow 13 \rightarrow 40	40 \rightarrow 13 \rightarrow 43	43 \rightarrow 13 \rightarrow 38
14	39 \rightarrow 14 \rightarrow 41	41 \rightarrow 14 \rightarrow 44	44 \rightarrow 14 \rightarrow 39	41 \rightarrow 14 \rightarrow 39	39 \rightarrow 14 \rightarrow 44	44 \rightarrow 14 \rightarrow 41
15	41 \rightarrow 15 \rightarrow 40	40 \rightarrow 15 \rightarrow 45	45 \rightarrow 15 \rightarrow 41	40 \rightarrow 15 \rightarrow 41	41 \rightarrow 15 \rightarrow 45	45 \rightarrow 15 \rightarrow 40
16	47 \rightarrow 16 \rightarrow 46	46 \rightarrow 16 \rightarrow 42	42 \rightarrow 16 \rightarrow 47	46 \rightarrow 16 \rightarrow 47	47 \rightarrow 16 \rightarrow 42	42 \rightarrow 16 \rightarrow 46
17	46 \rightarrow 17 \rightarrow 48	48 \rightarrow 17 \rightarrow 43	43 \rightarrow 17 \rightarrow 46	48 \rightarrow 17 \rightarrow 46	46 \rightarrow 17 \rightarrow 43	43 \rightarrow 17 \rightarrow 48
18	49 \rightarrow 18 \rightarrow 47	47 \rightarrow 18 \rightarrow 44	44 \rightarrow 18 \rightarrow 49	47 \rightarrow 18 \rightarrow 49	49 \rightarrow 18 \rightarrow 44	44 \rightarrow 18 \rightarrow 47
19	48 \rightarrow 19 \rightarrow 49	49 \rightarrow 19 \rightarrow 45	45 \rightarrow 19 \rightarrow 48	49 \rightarrow 19 \rightarrow 48	48 \rightarrow 19 \rightarrow 45	45 \rightarrow 19 \rightarrow 49
20	50 \rightarrow 20 \rightarrow 51	51 \rightarrow 20 \rightarrow 38	38 \rightarrow 20 \rightarrow 50	51 \rightarrow 20 \rightarrow 50	50 \rightarrow 20 \rightarrow 38	38 \rightarrow 20 \rightarrow 51
21	52 \rightarrow 21 \rightarrow 50	50 \rightarrow 21 \rightarrow 39	39 \rightarrow 21 \rightarrow 52	50 \rightarrow 21 \rightarrow 52	52 \rightarrow 21 \rightarrow 39	39 \rightarrow 21 \rightarrow 50
22	50 \rightarrow 22 \rightarrow 53	53 \rightarrow 22 \rightarrow 40	40 \rightarrow 22 \rightarrow 50	53 \rightarrow 22 \rightarrow 50	50 \rightarrow 22 \rightarrow 40	40 \rightarrow 22 \rightarrow 53
23	54 \rightarrow 23 \rightarrow 50	50 \rightarrow 23 \rightarrow 41	41 \rightarrow 23 \rightarrow 54	50 \rightarrow 23 \rightarrow 54	54 \rightarrow 23 \rightarrow 41	41 \rightarrow 23 \rightarrow 50
24	51 \rightarrow 24 \rightarrow 52	52 \rightarrow 24 \rightarrow 42	42 \rightarrow 24 \rightarrow 51	52 \rightarrow 24 \rightarrow 51	51 \rightarrow 24 \rightarrow 42	42 \rightarrow 24 \rightarrow 52
25	53 \rightarrow 25 \rightarrow 51	51 \rightarrow 25 \rightarrow 43	43 \rightarrow 25 \rightarrow 53	51 \rightarrow 25 \rightarrow 53	53 \rightarrow 25 \rightarrow 43	43 \rightarrow 25 \rightarrow 51
26	52 \rightarrow 26 \rightarrow 54	54 \rightarrow 26 \rightarrow 44	44 \rightarrow 26 \rightarrow 52	54 \rightarrow 26 \rightarrow 52	52 \rightarrow 26 \rightarrow 44	44 \rightarrow 26 \rightarrow 54
27	54 \rightarrow 27 \rightarrow 53	53 \rightarrow 27 \rightarrow 45	45 \rightarrow 27 \rightarrow 54	53 \rightarrow 27 \rightarrow 54	54 \rightarrow 27 \rightarrow 45	45 \rightarrow 27 \rightarrow 53
28	51 \rightarrow 28 \rightarrow 55	55 \rightarrow 28 \rightarrow 46	46 \rightarrow 28 \rightarrow 51	55 \rightarrow 28 \rightarrow 51	51 \rightarrow 28 \rightarrow 46	46 \rightarrow 28 \rightarrow 55
29	55 \rightarrow 29 \rightarrow 52	52 \rightarrow 29 \rightarrow 47	47 \rightarrow 29 \rightarrow 55	52 \rightarrow 29 \rightarrow 55	55 \rightarrow 29 \rightarrow 47	47 \rightarrow 29 \rightarrow 52
30	53 \rightarrow 30 \rightarrow 55	55 \rightarrow 30 \rightarrow 48	48 \rightarrow 30 \rightarrow 53	55 \rightarrow 30 \rightarrow 53	53 \rightarrow 30 \rightarrow 48	48 \rightarrow 30 \rightarrow 55
31	55 \rightarrow 31 \rightarrow 54	54 \rightarrow 31 \rightarrow 49	49 \rightarrow 31 \rightarrow 55	54 \rightarrow 31 \rightarrow 55	55 \rightarrow 31 \rightarrow 49	49 \rightarrow 31 \rightarrow 54

Note: The oriented boundary cubes have their centers at the predefined locations as pictured in Fig. 7.b. The start and end points of the 192 paths are potential points of ambiguity, as shown in Fig. 7.c. For the orientations, *cf.*, Appendix A.

3.4 Generation of a Single Tetrahedron

In this subsection, we shall demonstrate the extraction of an iso-hypersurface for a single toxel (*cf.*, Fig. 4.c). We also indicate the relevant processing stages (*cf.*, Fig. 3).

In 2D, a single pixel is represented within a 2×2 -neighborhood by a quarter of its (quadratic) area. In 3D, a single voxel is represented within a $2 \times 2 \times 2$ -neighborhood by an eights of its (cubic) volume.

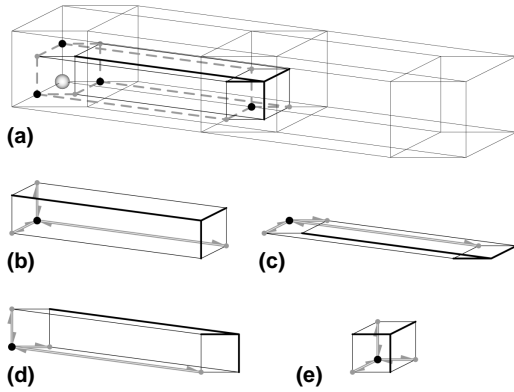


Fig. 8. (a) A sixteenth of a toxel within a 4D-cell at site no. 7; detailed views of the corresponding boundary volume octants (b) no. 11 \oplus ; (c) no. 9 \ominus ; (d) no. 6 \ominus ; (e) no. 18 \oplus (*cf.*, Table 2).

Analogously in 4D, a single toxel is represented within a $2 \times 2 \times 2 \times 2$ -neighborhood by a sixteenth of its (4-cubic) space-time¹⁰. Hence, we need sixteen different 4D-cells for the proper construction of the complete hypersurface of a single toxel. In order to demonstrate how STEVE uses the previously introduced indexing scheme (*cf.*, Fig. 7) in combination with the vector path table (*cf.*, Table 2), we shall process here a single sixteenth of a toxel.

As an example, we shall consider within a 4D-cell the four BVOs for the single toxel at site ID no. 7 (*cf.*, Fig. 8.a). These are the volumes no. 11 \oplus (in the positive x -direction; *cf.*, Fig. 8.b), no. 9 \ominus (in the negative y -direction; *cf.*, Fig. 8.c), no. 6 \ominus (in the negative z -direction; *cf.*, Fig. 8.d), and no. 18 \oplus (in the positive t -direction; *cf.*, Fig. 8.e). Hence, we have identified the initial paths (or TCV pairs; *cf.*, Fig. 3.c). In total we obtain 24 initial vectors (*cf.*, Fig. 9.a), which – in a next step – can be combined into the four initial cyclic (i.e., closed) vector paths, or the protomesh: 37 \rightarrow 9 \rightarrow 34 \rightarrow 6 \rightarrow 36 \rightarrow 11 \rightarrow 37, 36 \rightarrow 6 \rightarrow 44 \rightarrow 18 \rightarrow 49 \rightarrow 11 \rightarrow 36, 47 \rightarrow 9 \rightarrow 37 \rightarrow 11 \rightarrow 49 \rightarrow 18 \rightarrow 47, and 34 \rightarrow 9 \rightarrow 47 \rightarrow 18 \rightarrow 44 \rightarrow 6 \rightarrow 34, respectively (*cf.*, Fig. 3.e).

Note that at the junctures, TCVs are only connected such that the end-point of a predecessor connects to the starting-point of a linked successor (which *never* must be anti-

10. I.e., if we choose three spatial dimensions and a temporal one.

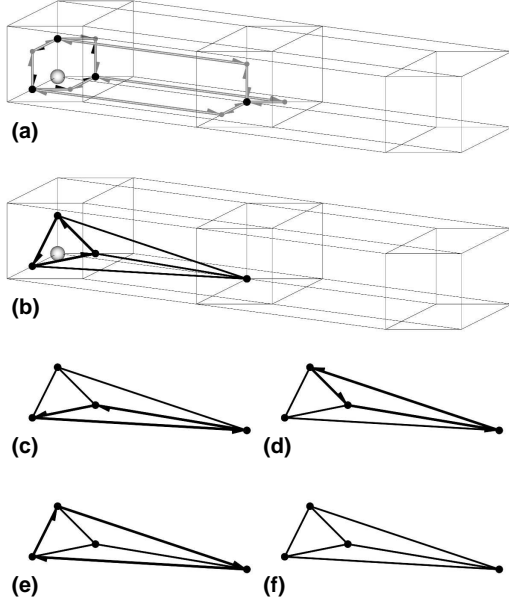


Fig. 9. Continuation of Fig. 8: (a) the four initial cyclic vector paths within a 4D-cell. The final tetrahedron together with the final cyclic vector path (b) $11 \rightarrow 9 \rightarrow 6 \rightarrow 11$ (embedded into the 4D-cell); (c) $11 \rightarrow 6 \rightarrow 18 \rightarrow 11$; (d) $18 \rightarrow 9 \rightarrow 11 \rightarrow 18$; (e) $6 \rightarrow 9 \rightarrow 18 \rightarrow 6$. (f) The final tetrahedron, where each of its edges represents a pair of anti-parallel vectors.

parallel to the preceding vector). The vector connectivities at the boundary cube centers are always predefined through the vector path table (cf., Table 2).

In a further step, all junctures (i.e., those with point IDs above 31, cf., Fig. 7.c) will be discarded (cf., Fig. 3.f). As a result, one obtains a single tetrahedron (cf., Fig. 3.h) that is represented by its four final, reduced cyclic vector paths (cf., Figs 9.b–f). Each of these cyclic vector paths represents a triangle, which is embedded into 4D. Note that the initial orientations of the boundary volumes have been passed on, such that a consistent evaluation of 4-normal vectors is possible (cf., Appendix A).

If we repeat the above processing for the remaining fifteen 4D-cells, we end up in total with sixteen oriented tetrahedrons that in their union represent the final STEVE-hypersurface for a single, isolated active toxel (cf., Fig. 10.c). The STEVE algorithm has stored at this stage the generated

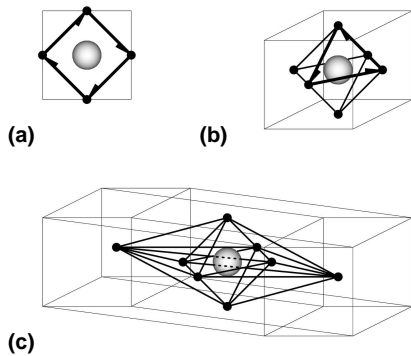


Fig. 10. Resulting manifolds of codimension 1 for a single (a) pixel in 2D, (b) voxel in 3D, and (c) toxel in 4D, respectively.

3-simplices (cf., Fig. 3.j) and thereby completes its processing. Note that in Fig. 10.c the orientations of the triangles of the tetrahedrons are not drawn, because in that 4D space each triangle is oriented in both ways.

For comparison we show in Fig. 10.a the DICONEX-contour – consisting of four vectors – for a single, isolated pixel [16]. And in Fig. 10.b, we show the VESTA-surface – consisting of eight oriented triangles – for a single, isolated voxel [12]. Note that each edge of the octahedron represents two anti-parallel vectors.

3.5 Isochronous Hypersurface Segments

While considering time as the fourth dimension, a so-called isochronous hypersurface segment (cf., Ref. [17], for an application) may be generated. It has a rather simple geometry within a given 4D-cell (i.e., similar to the generated single tetrahedrons in the previous subsection). If all eight toxel sites of the “past” are active, and simultaneously all eight toxel sites of the “future” are inactive (cf., Fig. 11), then one obtains as a result a cube-shaped segment (as shown in the figure at the intermediate time, here, the “present”), which simply fills the whole 3D space at the fixed time.

Note that here the initial eight BVOs yield after consideration of both the indexing scheme (cf., Fig. 7) and the vector path table (cf., Table 2), six initial cyclic vector paths, i.e., the protomesh. The orientations of the final vector paths are inherited from the initial ones (i.e., either \oplus or \ominus ; cf., Figs 6.e and 6.f, and Table 2) after the removal of the junctures. In Fig. 11.b, the tiny black arrows mark the initial TCVs, which lead to the final vector 4-cycles that are pronounced in Fig. 11.c.

3.6 Subspaces and Bounding Shapes

In the previous two subsections, we have encountered two rather simple 3D shapes as resulting hypersurface segments, i.e., a tetrahedron and a cube, respectively. The 4D-cells

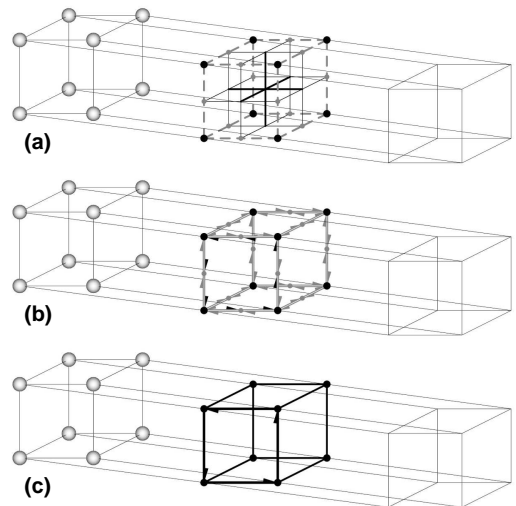


Fig. 11. Generation of an isochronous hypersurface segment within a 4D-cell: (a) initial boundary volume octants; (b) protomesh; (c) final cube-shaped hypersurface segment, with one final cyclic (clockwise oriented) vector path indicating the orientation of the hypersurface segment.

within which STEVE determines iso-hypersurface segments are each bounded by eight 3-cubes (or cubes), i.e., 3D subspaces (*cf.*, Appendix B). Both previously determined hypersurface segments, i.e., the tetrahedron and the cube, are themselves bounded by either four triangles (i.e., 3-cycles; *cf.*, Fig. 12.3) or six squares (i.e., 4-cycles; *cf.*, Fig. 12.4.b), respectively. Note that each triangle or square is embedded in a 3D subspace.

In fact, all possible hypersurface segments that the STEVE algorithm will generate are bounded by the N -cycles ($N = 3, 4, 5, 6, 7, 8, 9, 12$), which VESTA [12] would create, if it were processing the active voxels within properly arranged 3D-cells (i.e., $2 \times 2 \times 2$ -neighborhoods of voxels). This observation agrees with the fact that the number of vector paths (i.e., 192) for the STEVE algorithm (*cf.*, Table 2) equals to eight times of the number of vector paths (i.e., 8×24) for the marching variant of VESTA (*cf.*, Ref. [12]).

In 2D, the DICONEX [16] algorithm determines all properly oriented line segments within the cube-bounding 2D subspaces, i.e., its six squares. In Fig. 12, the complete tiling sets of segments of the manifolds of codimension 1 for 2D and 3D (sub)spaces as determined by the DICONEX, VESTA, and STEVE algorithms are pictured. Note that multiple segments could be generated within in a given (sub)space (for more detail, *cf.*, Ref. [12]).

3.7 Decomposition of Hypersurface Segments

This subsection addresses the decomposition of polytopes within the STEVE algorithm (*cf.*, Fig. 3.i). E.g., for visualization purposes and/or for the purpose of 4-normal vector calculations (*cf.*, Appendix A) one has to decompose the polytopes into a set of tetrahedrons (3-simplices) ¹¹.

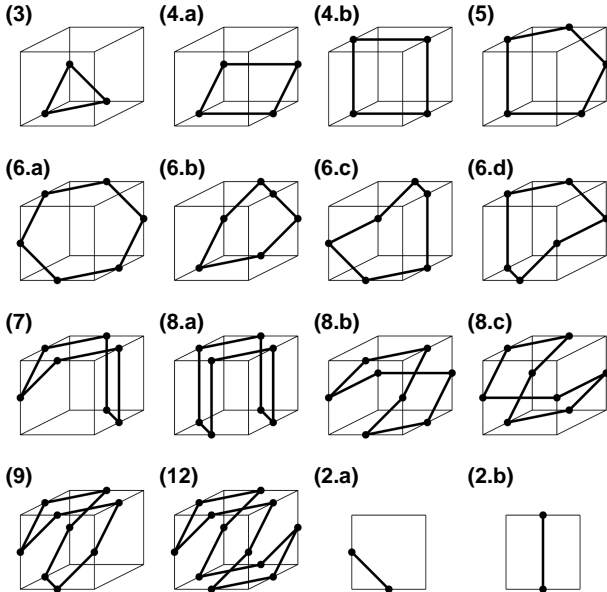


Fig. 12. Bounding shapes (tiling sets) for DICONEX, VESTA, and STEVE: (3) – (12) fourteen different 3D surface cycles for 3D (sub)spaces; (2.a) & (2.b) two different 2D contour segments for 2D (sub)spaces, which can be combined into polygons of the previous 3D-cells.

11. For more detail on the subject of polytope analysis, *cf.*, Ref. [18].

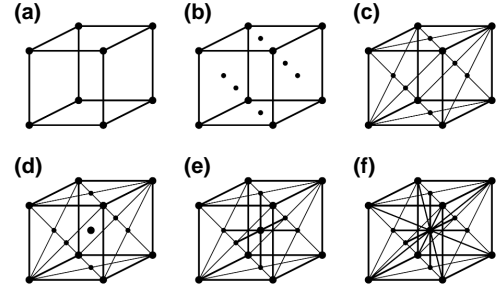


Fig. 13. High resolution decomposition of a cube into twenty-four tetrahedrons (see text).

Due to the various 3D bounding shapes as shown in Figs 12.3 – 12.12, the polytopes generated by STEVE could be very complex-shaped.

As an example, we demonstrate in Fig. 13, how to decompose a single cube into twenty-four tetrahedrons. Fig. 13.a shows a cube, which consists of six 3D tilings (4-cycles) as shown in Fig. 12.4.b. In Fig. 13.b, for each 4-cycle its center of mass point (face center) is marked. In Fig. 13.c, the surface cycles are decomposed into triangles while connecting the face centers with the corresponding 4-cycle support points. Each newly drawn line actually represents a pair of anti-parallel vectors. Note that neither triangles nor single tetrahedrons will be decomposed by us any further ¹².

Next, in Fig. 13.d, all triangles that enclose a particular single volume are collected into an object along with the information, to which N -cycles the triangles belong; furthermore, the absolute center of the enclosed volume is determined. In Fig. 13.e, lines are introduced that connect the face centers with the absolute volume center. Finally, in

12. However, this is done so, e.g., in Ref. [11].

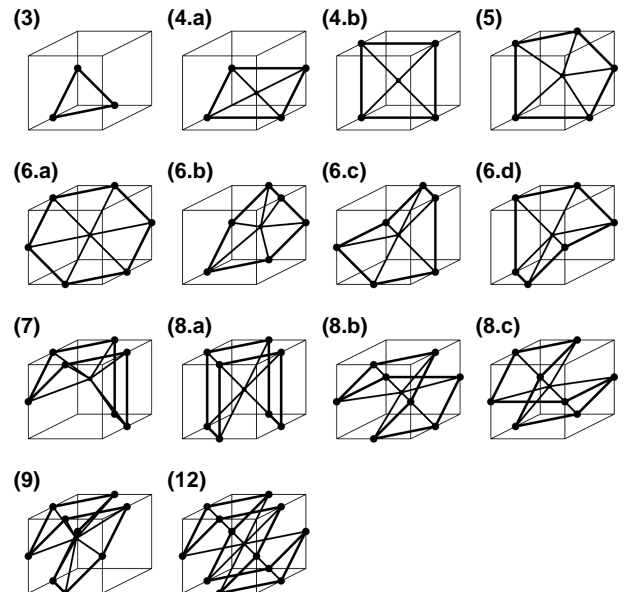


Fig. 14. High resolution decomposition of the 3D bounding shapes (tiling sets) for VESTA, and STEVE (*cf.*, Fig. 12).

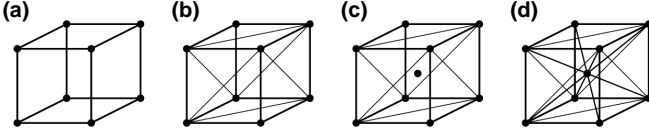


Fig. 15. Low resolution decomposition of a cube into twelve tetrahedrons (see text).

Fig. 13.f, the additional connections of all 4-cycle support points with the absolute volume center finally yields the twenty-four properly oriented tetrahedrons. In Fig. 14, we show the high resolution decompositions of all possible 3D tiling sets.

As an alternative, we show in Fig. 15 a lower resolution decomposition that is similar to the previous one. In particular, the steps that are shown in Figs 13.b and 13.c are replaced by N -cycle decompositions, which do not have any additional center of mass points (cf., Ref. 15.b). Hence, in Fig. 15 the step that is shown in Fig. 13.e is omitted. This latter procedure only yields twelve, but also properly oriented tetrahedrons. In Fig. 16, we show the low resolution decompositions of all possible 3D tiling sets.

Within STEVE, one can use both – i.e., high resolution (HR), and low resolution (LR) – types of decompositions into 3-simplices for the potentially complex shaped polytopes. Note that the polytopes, which are embedded into 4D, could be decomposed also while using fewer tetrahedrons. E.g., one could decompose a cube into just five tetrahedrons. However, the usage of fewer tetrahedrons could introduce stronger directional dependencies into the hypersurface (cf., application subsection 4.4).

3.8 Generation of a Triangular Strut

In another example, we briefly demonstrate the generation of a hypersurface segment that has the shape of a triangular

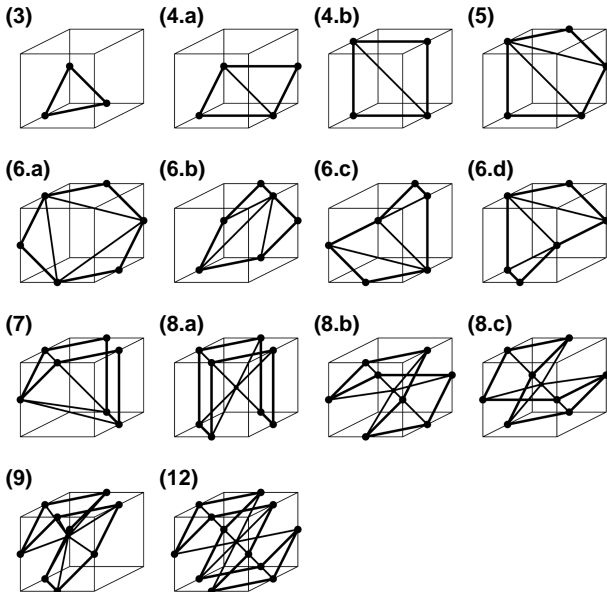


Fig. 16. Low resolution decomposition of the 3D bounding shapes (tiling sets) for VESTA, and STEVE (cf., Fig. 12).

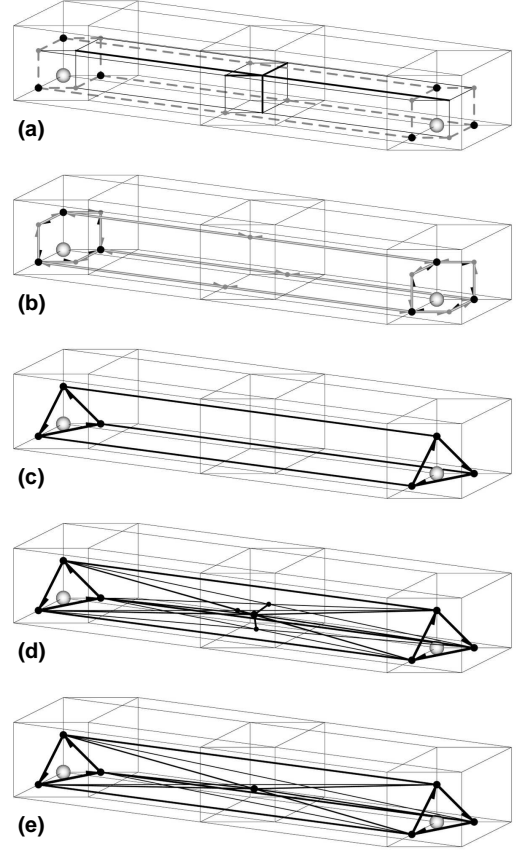


Fig. 17. Generation of a triangular strut within a 4D-cell (see text).

strut. In Fig. 17, two toxels (in NV) at site IDs no. 7 and no. 15 are in contact through a single volume. This volume of contact is visible within the cube that represents here the “present” (cf., Fig. 17.a). It actually is made up by the superposition of two BVOs that each have opposite orientations, i.e., no.s $18 \oplus$ and $18 \ominus$ (in the positive and negative t -directions, respectively). Hence, their TCVs *cancel out* each one another, and there is no contribution to the protomesh from this volume.

Once again, the application of both, the indexing scheme (cf., Fig. 7) and the vector path table (cf., Table 2), yields five initial cyclic vector paths (cf., Fig. 17.b), i.e., the protomesh. Fig. 17.c shows the final triangular strut-shaped hypersurface segment, with two final cyclic vector paths indicating its orientation. Note that this segment is bounded by two 3-cycles as shown in Fig. 12.3, and by three 4-cycles as shown in Fig. 12.3.a, respectively. Finally, in Figs 17.d and 17.e, we picture HR- and LR-decompositions of the hypersurface segment into fourteen and eight oriented tetrahedrons, respectively (cf., Figs 13 and 15).

For this particular example, the STEVE algorithm made use of all processing steps that are indicated in the flowchart (cf., Fig. 3) except for the support point interpolation and the identification of POAs (cf., Figs 3.g and 3.d, respectively). Since we did not yet encounter any particular topological ambiguities while constructing hypersurface segments, we are going to discuss their treatment next.

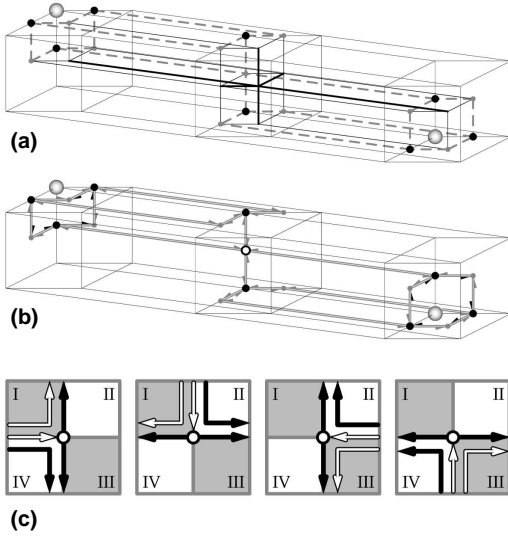


Fig. 18. Encounter of a topological ambiguity within a 4D-cell: (a) initial boundary cubes; (b) protomesh; (c) connectivity diagram.

3.9 Ambiguous Connectivity

The discretized spaces that we consider here could lead to topological ambiguities. In 2D this is the case, if two active pixels share only one common point (i.e., a vertex; *cf.*, Ref. [16] for more detail). In 3D this is the case, if two active voxels share only one common edge (*cf.*, Ref. [12] for more detail). Analogously, this is the case in 4D, if two active toxels share only one common face (square).

In Fig. 18.a, we show a 4D-cell with two active toxels at site IDs No. 4 and No. 15. The (sixteenth of the) toxels are in contact through a single face. Within the cube that here represents the “present” this surface of contact is visible. It actually is made up by the contact of the two neighboring BVOs no.s $16 \oplus$ and $18 \ominus$ (in the positive and negative t -directions, respectively). In particular for both BVOs, their paths no.s 1 and 3 (*cf.*, Table 2) start and end at juncture no. 47, respectively (*cf.*, Fig 3.d).

Hence, we have in Fig. 18.b an ambiguous configuration (white dot) for the protomesh. Evidently, this particular juncture has turned into a so-called “point of ambiguity” (POA; *cf.*, Ref. [12]). The connectivity diagram (*cf.*, Fig. 18.c) helps to consistently resolve which preceding TCV should connect to a succeeding TCV. Each incoming (white, straight) vector can connect to either one of the two (black, straight) vectors, depending on the chosen connectivity mode. Using the field values for the toxels at positions I , II , III , and IV in the figure, one may assign their average field value to the POA.

E.g., for an average field value below (above) the desired iso-value of the hypersurface, one generates the local “disconnect” (“connect”) mode while pursuing the white (black) bent directed path for each incoming vector consistently. This latter treatment (also known as “mixed” mode [12] treatment) will allow for an automated, robust resolution of all encountered ambiguities. Note that one may enforce the connectivity modes also globally onto the complete considered 4D data set, by either *always* selecting the “disconnect”, or the “connect” mode.

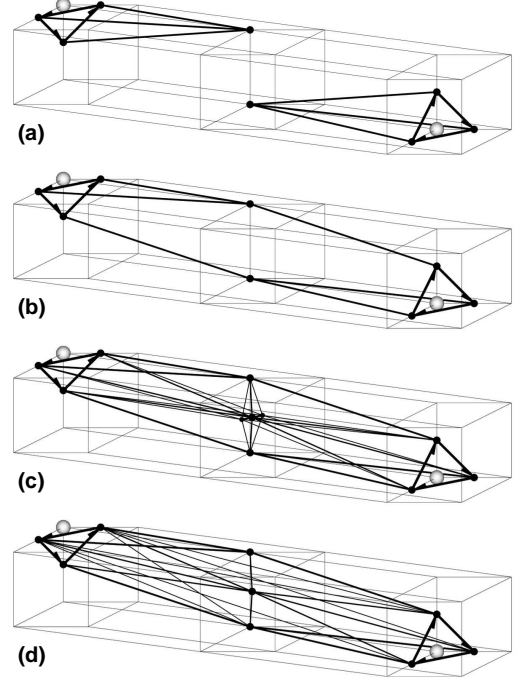


Fig. 19. Continuation of Fig. 18: (a) two resulting tetrahedrons from the “disconnect” mode; (b) a final, more complex-shaped hypersurface segment, resulting from the “connect” mode; (c) as in (b), but with a hypersurface segment decomposition into sixteen tetrahedrons. (d) as in (c), but with a decomposition into twelve tetrahedrons only.

In Fig. 19.a, we show two final hypersurface segments (tetrahedrons) that result from the “disconnect” mode. Alternatively, we show in Fig. 19.b one final hypersurface segment that results from the “connect” mode. This single segment is bounded by four 3-cycles as shown in Fig. 12.3, and by two 6-cycles as shown in Fig. 12.6.b, respectively. In Fig. 19.c, it has been HR-decomposed (*cf.*, Fig. 13) into sixteen oriented tetrahedrons, and in Fig. 19.d, it has been LR-decomposed (*cf.*, Fig. 15) into just twelve oriented tetrahedrons. Note that each drawing in Fig. 19 shows two final cyclic vector paths indicating the orientation of the hypersurface segments.

We would like to stress that due to the here considered *discretized* 4D spaces, STEVE can generate *six different* types of hypersurfaces: both high (i.e., HR) and low (i.e., LR) resolution hypersurfaces, each one of them in either “mixed”, or global “disconnect” and “connect” modes.

3.10 Disjunct Hypersurface Segments

In 3D, VESTA never connects two voxels that are in contact only through a single vertex (*cf.*, Ref. [12] for more detail). In 4D, we have a similar situation when considering toxels that are in direct contact.

In Figs 20 and 21, the process of hypersurface segment generation (*cf.*, Ref. 3) is shown for two toxels that are in contact only through a single edge and through a single vertex, respectively. In both cases, we simply obtain two tetrahedrons as final hypersurface segments, since the initial cyclic vector paths form two disjunct sets with four cyclic paths each. Apparently, toxel pairs with such a weak connectivity will always result in two separate hypersurface segments. This concludes the technical section of this paper.

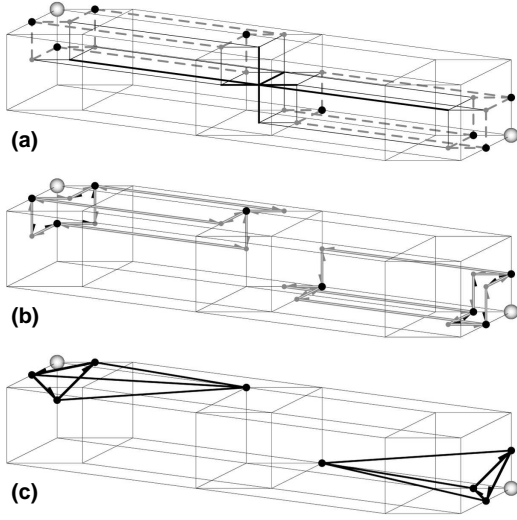


Fig. 20. Hypersurface segment generation for two toxels, which are in contact through a single edge: (a) initial boundary cubes; (b) two disjunct protomeshes; (c) two resulting tetrahedrons.

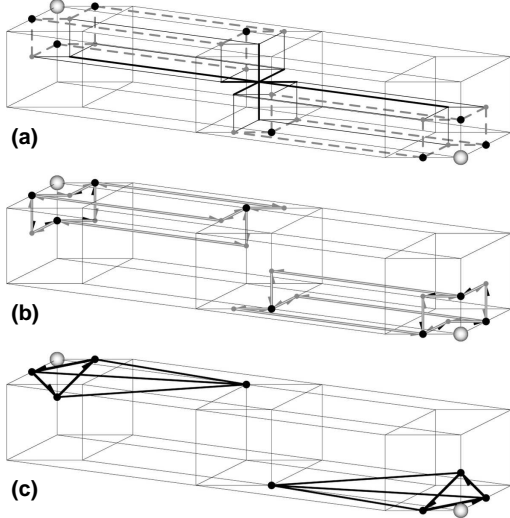


Fig. 21. Hypersurface segment generation for two toxels, which are in contact through a single vertex: (a) initial boundary cubes; (b) two disjunct protomeshes; (c) two resulting tetrahedrons.

4 APPLICATIONS

In this application section, we present various examples for hypersurface generation in 4D.

These are (i) the shape characterization of a 4D transversal phase space in the field of ion beam transport, (ii) the continuous transmutation of a square into two triangles, (iii) the isotherme evolution of a fireball expansion in the field of relativistic heavy-ion physics, and (iv) the study of intersections of low and high resolution hypersurfaces for a shrinking sphere.

4.1 4D Shape Characterization

In the field of accelerator physics, for charged particle beams both tomographic reconstructions (*cf.*, e.g., Ref. [19]) and simulation data (*cf.*, e.g., Ref. [20]) of the 4D transverse phase

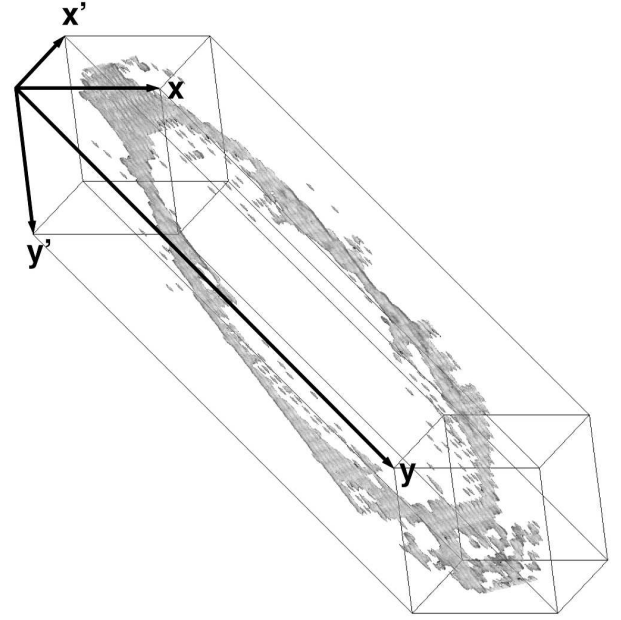


Fig. 22. Projection of the full 4D hypersurfaces (i.e., volumes) generated by STEVE in the 4D transversal phase space of a charged particle beam (see text).

space are available. Accelerator physicists characterize the beams typically by using beam ellipsoids (*cf.*, e.g., Ref. [21]), while assuming that there is a decoupling between the radial and axial components in the transverse plane. However, in reality this assumption may be unwarranted because the occupied phase space may have a quite different shape due to non-linear effects. STEVE can help to visualize the particular phase space shape.

In Fig. 22, we show a projection of the full hypersurfaces that result from the application of the STEVE algorithm to the 4D phase space simulation data that have been presented in Ref. [20]. STEVE generates for this $50 \times 50 \times 50 \times 50$ -sized toxel data set with an iso-value of 1 (i.e., it is enclosing all entries larger than 0 in the grid) 129,563 tetrahedrons in its high resolution “mixed” mode. In the figure, x and y denote the radial and axial deviations from the ideal beam position in the transversal plane, whereas x' and y' denote the corresponding angles, respectively. Interpolations have *not* been applied here to the 102,037 4D support points.

4.2 Bifurcation within a 4-Cell

Typically, the meshes of tetrahedrons that represent the final hypersurfaces are very dense. In order to learn more about their inherent shape features, it is useful to intersect the generated manifolds with a 3D space at a certain fixed value. E.g., one could keep the fourth dimension (which we have named time here) at a particular fixed value and then visualize the resulting shape. Note, that such shapes could consist of single points, line segments, triangles, quadrilaterals, and/or (the whole volume of intersected) tetrahedrons (*cf.*, the isochronous hypersurface segments, above).

In Fig. 23, we show a sequence of one and the same 4D-cell (i.e., in NV) with six activated toxel sites each. In the “past” the four toxels with IDs 4, 5, 6 and 7 are active, whereas in the “future” the two toxels with IDs 12 and

14 are active (*cf.*, Fig. 7.a). STEVE has been applied to this configuration in its global high resolution “disconnect” mode, in order to determine the hypersurface section (i.e., the network of black lines in the figure). For each tesseract (except for the first and the last one), an additional cube is drawn for various fixed times t . The parameter, t , denotes a relative value that ranges between the extremes of 0 and 1 for intersections.

For the generated hypersurface segment, Fig. 23 shows an evolution of surface segments as a result of the chosen intersections. Here it is demonstrated, how a single square may transform continuously and smoothly into two separated triangles. The pictured 4D hypersurface segment (i.e., 32 tetrahedrons) establishes a correspondence between the surfaces in the “past” and in the “future” (and between those anywhere in between).

4.3 Isotherme Evolution

The quest for the correct equation of state of nuclear matter continues (*cf.*, e.g., Ref. [22] and Ref.s therein). E.g., relativistic hydrodynamical models that simulate relativistic heavy ion collisions are employed for its particular characterization [23], [24]. In doing so, one may be faced with the task of freezeout hypersurface (FOHS) extraction from 3 + 1D hydrodynamic simulation data (*cf.*, e.g., Ref. [25] and Ref.s therein). In this example, a relativistic fluid has been propagated numerically on a cartesian 3D grid.

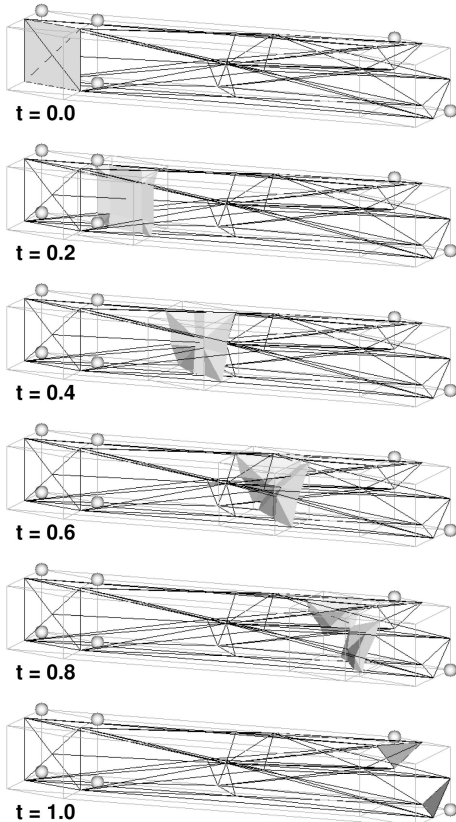


Fig. 23. Continuous transformation of a single quadrilateral into two separate triangles (see text).

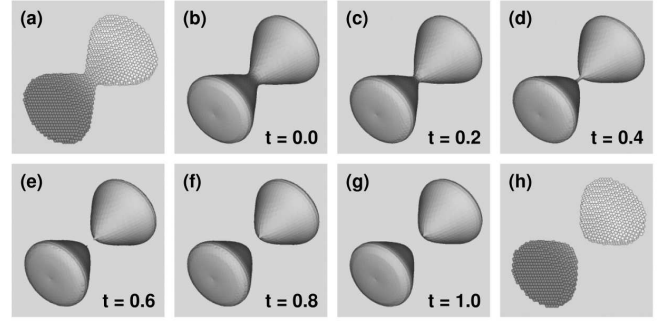


Fig. 24. Generation of chronologically developing isothermes: (a) & (h) selected grid cells of the discretized 3D temperature fields at two subsequent time steps; (b) – (g) various temporal hypersurface intersections.

The spheres in Fig.s 24.a and 24.h represent grid cells above a certain threshold temperature at two subsequent time steps (in GV) for the here considered fireball of hot, dense nuclear matter that decays into two pieces. For visualization purposes, STEVE has been used (in its high resolution global “disconnect” mode) in order to determine the (continuous) isothermal hypersurface that lies between the two shown 3D data sets. Various temporal intersections within the bounds given by Fig.s 24.a and 24.h are shown here for illustration.

Note that the 4D support point set has been interpolated linearly. In particular, STEVE provides interpolations for all other field values that have been associated with each toxel as well. For the purpose of FOHS extraction, STEVE will not just be applied to two subsequent time steps as shown in the figure, but to any full set of 4D simulation data. The resulting total FOHS will allow for calculations of so-called observables (*cf.*, e.g., Ref. [26]).

4.4 High vs. Low Resolution Rendering

In this subsection, we discuss the effects of choosing a lower resolution for the decomposition (*cf.*, Fig.s 15 and 16 vs. Fig.s 13 and 14) of the polytopes generated by STEVE. In Fig.s 25 and 26, we each show the same two pairs of (i.e., without any noise) constructed volumetric data. Both sets of data represent massive spheres, where the second sphere has a slightly smaller radius. For the union of the two 3D data sets (i.e., 4D data) both a HR- and a LR-hypersurface have been generated with STEVE.

These have been intersected in the same manner as the FOHS segment of the previous subsection. Note that the lower resolution decomposition leads to additional artifacts in the resulting surfaces (*cf.*, Fig.s 26.c through 26.f). We would like to emphasize that, e.g., a 4D generalization of the (extended) Marching Cubes algorithm [28], [29] would generate such artifacts, because it provides only lower resolution surface templates.

5 IMPLEMENTATION ISSUES

The original Marching Cubes algorithm (MCA) by Lorenzen and Cline [28] used only fourteen templates for the construction of surfaces from 3D volumetric images. This algorithm had to be extended, because the number of templates was *insufficient*, i.e., it could not warrant final surfaces that do not contain any holes. An implementation of the extended

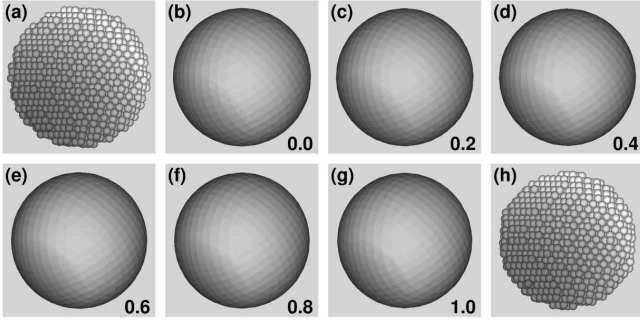


Fig. 25. A shrinking sphere: (a) & (h) selected grid cells for two, i.e., initial and final, 3D data sets; (b) – (g) various intersections of the generated high resolution iso-hypersurface; the numbers refer to the intersection parameter, t .

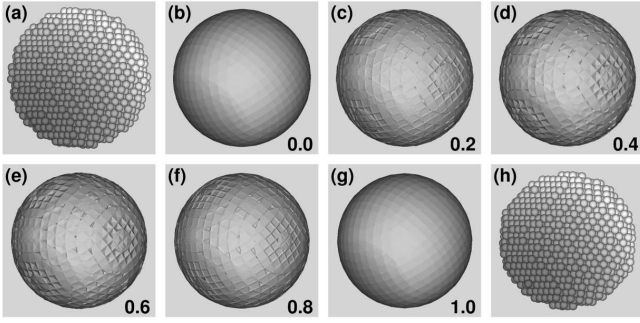


Fig. 26. As in Fig. 25, but for a generated iso-hypersurface of lower resolution. Note the additional artifacts at intersections (c) – (f).

MCA can be found in Ref. [29]. However, in order to obtain an efficient look-up table based computer program, 256 configurations (*cf.*, Table 3) – rather than only 17 – are implemented.

In contrast, VESTA only requires the storage of half of the 24 directed paths (*cf.*, Table 1), due to its \oplus/\ominus -symmetry. Note that the extended MCA generates the exact surfaces as VESTA, if the latter is executed in its low-resolution “disconnect” mode [12]. I.e., unlike VESTA the MCA *cannot*

be considered data-driven, because it cannot deal with a “mixed” connectivity mode. E.g., the MCA cannot produce the 3D surface tiles as shown in Figs 16.8.a – 16.12.

The authors of Ref. [8] state that they only require 222 configurations to provide templates for building hypersurfaces in 4D. However, these 222 configurations are used to fill a 2^{16} -sized (i.e., 65,536-sized) look-up table, whereas STEVE only requires the storage of half of the 192 directed paths (*cf.*, Tables 2 and 3), due to its \oplus/\ominus -symmetry.

If we consider even higher dimensions, due to Table 3 it would be quite impossible to provide a template based hypersurface generator – in the strict sense – for instance for a 11-dimensional M-Theory, whereas our technology [1] would not run into resource problems that easily.

6 SUMMARY

In summary, the 4D protomesh-based iso-hypersurface construction algorithm STEVE has been described here for the very first time in great detail. The STEVE algorithm basically requires the storage of 192 vector paths only. A minimum of data redundancy is achieved by avoiding the multiple counting of the manifold supporting points within the 4D-cells.

We would like to stress that there is *more than one* iso-hypersurface solution. This fact has not been pointed out explicitly by other authors yet. It is a consequence of the discretization of the 4D spaces under consideration, where topological ambiguities will allow for two different global treatments, and/or an additional local treatment, which is purely data-driven. The proper treatment of possible ambiguities warrants that accidental rifts in the final hypersurfaces *cannot be created*.

STEVE constructs iso-hypersurfaces while using a *single* 4D building block (*cf.*, e.g., Fig. 6.d). It continuously transforms the set of initially identified octants of boundary cubes into the final set of tetrahedrons. One can choose between both a high and a lower resolution decomposition of the generated polytopes. This final set of tetrahedrons represents one or more hypersurfaces. Note that the initially given information about the interior/exterior of the enclosed 4D regions will be propagated to the final results.

ACKNOWLEDGEMENTS

Some initial work has been supported by the Department of Energy under contract W-7405-ENG-36. At the time, the particular funding has resulted in a first version of ANSI C-based software [30], where ambiguities are resolved globally only. The author wishes to thank the organizers of the mini workshop on “Freeze-Out”, which was held at the Institute for Theoretical Physics, Goethe-University of Frankfurt, Germany, on May 6th, 2009, for the opportunity to give a talk on this research.

APPENDIX A PATH ORIENTATIONS

In Fig. 27, we show normalized normal vectors in 2D, 3D, and 4D, respectively, which are attached to the centers of selected oriented $(N - 1)$ -simplices. Each one of the

TABLE 3
Number of directed paths vs. number of templates as a function of integral dimension, N

No. of Paths		No. of Templates	
3D	(VESTA) 24	(MCA)	256
4D	(STEVE) 192		65,536
5D	1920		4,294,967,296
6D	23,040		$\approx 1.845 \times 10^{19}$
7D	322,560		$\approx 3.403 \times 10^{38}$
8D	5,160,960		$\approx 1.158 \times 10^{77}$
9D	92,897,280		$\approx 1.341 \times 10^{154}$
10D	1,857,945,600		$\approx 1.798 \times 10^{308}$
11D	40,874,803,200		$\approx 3.232 \times 10^{616}$
ND	$\prod_{k=2}^N 2k$		2^{2^N}

Note: The estimated number of atoms in our universe is $\sim 10^{80}$ (*cf.*, Ref. [27]).

simplices encloses an active N -dimensional picture element site with ID 0 within the shown $2(\times 2)^{N-1}$ -neighborhoods. In particular, the normalized normal vectors point to the exterior of the enclosed N -dimensional regions, i.e., each component of the normal vectors is larger than zero. The orientations of normal vectors depend on the orientations of the corresponding simplices, and vice versa. Hence, the orientations of the initial protomesh building block vectors depend on the orientations of the normal vectors.

Let the coordinate systems be chosen here as shown in Fig. 4. The demand that all components of the normal vectors should be larger than zero leads to the orientation of the contour vector (black arrow) in 2D and the orientation of the triangle (triplet of black vectors) in 3D as shown in Figs. 27.a and 27.b, respectively. In particular, the \oplus/\ominus naming convention of Table 1 becomes apparent for 3D. In 4D (similar to the lower dimensional cases), the particular choices depend on the way a 4D normal (or 4-normal) vector is constructed.

In application subsection 4.3, 4D space-time plays a vital role. Therefore, we consider first the more complex situation of relativity. Let $x^\mu = (x, y, z, t)$ be a contravariant event with the three spatial cartesian components x, y , and z , and the time t , respectively. I.e.,

$$x^\mu = x \mathbf{e}_x + y \mathbf{e}_y + z \mathbf{e}_z + t \mathbf{e}_t, \quad (1)$$

while considering the *canonical* multilinear basis

$$\begin{aligned} \{\mathbf{E}_i\} = \{ & 1, \mathbf{e}_x, \mathbf{e}_y, \mathbf{e}_z, \mathbf{e}_t, \mathbf{e}_x \wedge \mathbf{e}_y, \\ & \mathbf{e}_x \wedge \mathbf{e}_z, \mathbf{e}_x \wedge \mathbf{e}_t, \mathbf{e}_y \wedge \mathbf{e}_z, \mathbf{e}_y \wedge \mathbf{e}_t, \mathbf{e}_z \wedge \mathbf{e}_t, \\ & \mathbf{e}_x \wedge \mathbf{e}_y \wedge \mathbf{e}_z, \mathbf{e}_x \wedge \mathbf{e}_y \wedge \mathbf{e}_t, \mathbf{e}_x \wedge \mathbf{e}_z \wedge \mathbf{e}_t, \\ & \mathbf{e}_y \wedge \mathbf{e}_z \wedge \mathbf{e}_t, \mathbf{e}_x \wedge \mathbf{e}_y \wedge \mathbf{e}_z \wedge \mathbf{e}_t \}, \\ & i = 1, \dots, 16. \end{aligned} \quad (2)$$

The covariant event, $x_\mu = g_{\mu\nu} x^\nu$, can be obtained with the help of the metric tensor $g_{\mu\nu}$ that we assume here to be diagonalized, i.e., $g_{\mu\nu} = \text{diag}(g_{11}, g_{22}, g_{33}, g_{44})$. E.g., with $g_{11} = g_{22} = g_{33} = -1$ and $g_{44} = +1$, it follows that $x_\mu = (-x, -y, -z, t)$.

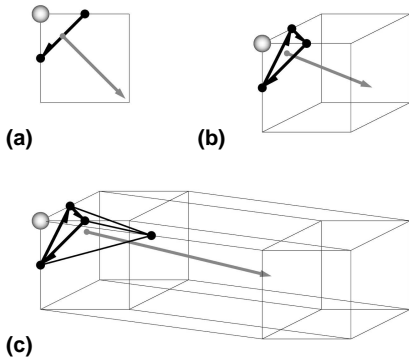


Fig. 27. Normalized normal vectors (gray) that are attached to the centers of the oriented $(N-1)$ -simplices, which enclose the active N -dimensional picture element sites with ID 0 within the shown N D-cells: (a) in 2D (b) in 3D, and (c) in 4D, respectively.

For the four given events $x_1^\mu = (x_1, y_1, z_1, t_1)$, $x_2^\mu = (x_2, y_2, z_2, t_2)$, $x_3^\mu = (x_3, y_3, z_3, t_3)$, and $x_4^\mu = (x_4, y_4, z_4, t_4)$, we form the differences

$$\begin{aligned} dx_1 &= x_2 - x_1, \quad dx_2 = x_3 - x_1, \quad dx_3 = x_4 - x_1, \\ dy_1 &= y_2 - y_1, \quad dy_2 = y_3 - y_1, \quad dy_3 = y_4 - y_1, \\ dz_1 &= z_2 - z_1, \quad dz_2 = z_3 - z_1, \quad dz_3 = z_4 - z_1, \\ dt_1 &= t_2 - t_1, \quad dt_2 = t_3 - t_1, \quad dt_3 = t_4 - t_1. \end{aligned} \quad (3)$$

Let us define the determinants

$$dS^{ikl} = \begin{vmatrix} dx_1^i & dx_2^i & dx_3^i \\ dx_1^k & dx_2^k & dx_3^k \\ dx_1^l & dx_2^l & dx_3^l \end{vmatrix}, \quad i, k, l \in \{1, 2, 3, 4\} \quad (4)$$

where $dx_m^1 = dx_m$, $dx_m^2 = dy_m$, $dx_m^3 = dz_m$, $dx_m^4 = dt_m$, $m = 1, 2, 3$.

E.g., while using Geometric Algebra (cf., e.g., Ref. [31]) one can show that the contravariant 4-normal is given through

$$d\sigma^\mu = \frac{1}{6} \left(\frac{dS^{234}}{g_{11}}, \frac{dS^{143}}{g_{22}}, \frac{dS^{124}}{g_{33}}, \frac{dS^{132}}{g_{44}} \right). \quad (5)$$

Note that the corresponding covariant 4-normal,

$$d\sigma_\mu = g_{\mu\nu} d\sigma^\nu = \frac{1}{6} (dS^{234}, dS^{143}, dS^{124}, dS^{132}), \quad (6)$$

does not depend on the 4D metric under consideration. For the special case of an isochronous hypersurface, i.e., $dt_1 = dt_2 = dt_3 = 0$ (cf., subsection 3.5, and Eq. (3)), we get

$$d\sigma_\mu = \frac{1}{6} (0, 0, 0, dS^{132}), \quad (7)$$

where $dS^{132} = -dS^{123}$, i.e., dS^{132} equals the *negative* volume of a parallelepiped that is spanned by the contravariant 4-vectors $dx_m^\mu = (dx_m, dy_m, dz_m, 0)$, $m = 1, 2, 3$. Eventually, while not considering relativity, i.e., $g_{\mu\nu} = \text{diag}(+1, +1, +1, +1)$, both $d\sigma^\mu$ and $d\sigma_\mu$ become identical, i.e., $d\sigma^\mu \equiv d\sigma_\mu$.

The previous evaluations have led to the particular \oplus/\ominus naming convention of Table 2 used in 4D. The chosen orientations therein, together with the particular choices of Eqs. (2) and (3) yield a 4-normal vector with all of its components larger than zero for the oriented tetrahedron shown in Fig. 27.c.

APPENDIX B SUBSPACE ORIENTATIONS

A tesseract is bounded by eight cubes. In Fig. 28, we picture the eight bounding cubes (or 3D subspaces) of the tesseract shown (in NV) in Fig. 7 at fixed components, $x_0, x_1, y_0, y_1, z_0, z_1, t_0$, and t_1 . The indices 0 and 1 refer to the minimum and maximum bounds of the corresponding dimensions, respectively. Each 3D subspace is labeled here with toxel site IDs (cf., Fig. 7.a), boundary cube centers (cf., Fig. 7.b), and junctures (cf., Fig. 7.c). Note that the subspaces at $x_{0/1}, y_{0/1}, z_{0/1}$, and $t_{0/1}$, are directly proportional to the basis 3-blades $\mathbf{E}_{15}, \mathbf{E}_{14}, \mathbf{E}_{13}$, and \mathbf{E}_{12} , respectively (cf., Fig. 28 and Eq. (2)).

If one applies the marching variant of VESTA [12] to

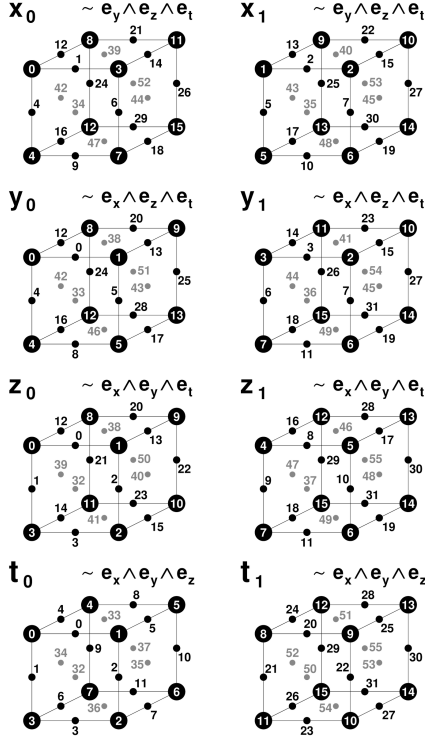


Fig. 28. 3D subspaces for the 4D-cell shown in Fig. 7. Note that the indices for voxels (white), boundary cube centers (black), and junctures (gray), coincide with the indexing as shown in Figs. 7.a – 7.c. The 3-blades are elements of the canonical multilinear basis, Eq. (2) (see text).

each one of these eight subspaces, one can emulate the processing steps of the STEVE algorithm as shown in Figs. 3.b through 3.g. However, because of

$$\begin{aligned} e_x \wedge e_y \wedge e_z \wedge e_t &= e_x \wedge \mathbf{E}_{15} = e_y \wedge (-\mathbf{E}_{14}) \\ &= e_z \wedge \mathbf{E}_{13} = e_t \wedge (-\mathbf{E}_{12}) \quad , \quad (8) \end{aligned}$$

one then has *by all means* to choose inverse orientations for the generated VESTA N -cycles in the x_0 -, y_1 -, z_0 -, and t_1 -subspaces. Only this warrants the consistent, orientation preserving construction of the higher-dimensional polytopes (*cf.*, Fig. 3.h).

REFERENCES

- [1] B. R. Schlei, "Verfahren zur Hyperflächenkonstruktion in n Dimensionen," german patent applications No. 10 2011 050 721.3 and No. 10 2011 051 203.9, submitted on May 30, 2011, and June 20, 2011, and PCT application No. PCT/EP2012/058873 submitted on May 14, 2012, by GSI Helmholtzzentrum für Schwerionenforschung GmbH, Planckstr. 1, 64291 Darmstadt, Germany, respectively.
- [2] X. A. Li, Editor, *Adaptive Radiation Therapy (Imaging in Medical Diagnosis and Therapy)*, CRC Press Inc. 2011.
- [3] A. Mundt, J. Roeske, *Image-Guided Radiation Therapy (IGRT): A Clinical Perspective*, McGraw-Hill Professional 2011.
- [4] S. S. Lo, B. S. Teh, J. J. Lu, T. E. Scheffer, Editors, *Stereotactic Body Radiation Therapy (Medical Radiology / Radiation Oncology)*, Berlin: Springer 2012.
- [5] Márta Fidrich, "Iso-Surface Extraction in 4D with Applications related to Scale Space," *Unité de recherche INRIA Sophia-Antipolis, Rapport de Recherche No. 2833, Programme 4*, March 1996.
- [6] C. Weigle, D. Banks, "Complex-Valued Contour Meshing," *Proceedings of Visualization '96*, San Francisco (1996) 173 – 80.
- [7] C. Weigle, D. Banks, "Extracting Isovalued Features in 4-Dimensional Scalar Fields," *Proceedings of 1998 Symposium on Volume Visualization*, Research Triangle Park (1998) 103 – 10.
- [8] P. Bhaniramka, R. Wenger, R. Crawfis, "Isosurface Construction in Any Dimension Using Convex Hulls," *IEEE Trans. Visualization and Computer Graphics* **10** (2004), doi: 10.1109/TVCG.2004.1260765.
- [9] J.-O. Lachaud, A. Montanvert, "Continuous Analogs of Digital Boundaries: A Topological Approach to Iso-Surfaces," *Graphical Models* **62** (2000) 129 – 64.
- [10] B. R. Schlei, "Hyper-Surface Extraction in Four Dimensions," *Theoretical Division - Self Assessment, Special Feature*, a portion of LA-UR-04-2143, Los Alamos (2004) 168.
- [11] P. Huovinen, H. Petersen, "Particization in Hybrid Models," *Eur. Phys. J. A* (2012) **48**, p. 171, doi: 10.1140/epja/i2012-12171-9.
- [12] B. R. Schlei, "Volume-Enclosing Surface Extraction," *Computers & Graphics* **36** (2012) 111 – 130, doi: 10.1016/j.cag.2011.12.008.
- [13] H. S. M. Coxeter, *Regular Polytopes*. Dover, 1973.
- [14] W. Boehm, M. Paluszny, H. Prautzsch, *Bezier and B-Spline Techniques*, Springer, Berlin, 2002.
- [15] D. Salomon, *Curves and Surfaces for Computer Graphics*, Springer, Berlin, 2005.
- [16] B. R. Schlei, "A New Computational Framework for 2D Shape-Enclosing Contours," *Image and Vision Computing* **27** (2009) 637 – 647, doi: 10.1016/j.imavis.2008.06.014.
- [17] H. Petersen, J. Steinheimer, G. Burau, M. Bleicher, H. Stöcker, "A Fully Integrated Transport Approach to Heavy Ion Reactions with an Intermediate Hydrodynamic Stage," *Phys. Rev. C* **78**, 044901 (2008).
- [18] E. Gawrilow, M. Joswig, "polymake: a framework for analyzing convex polytopes," *Polytopes – combinatorics and computation* (Oberwolfach, 1997), 43 – 73, DMV Sem. **29**, Birkhäuser, Basel, 2000, MR1785292 (2001f:52033).
- [19] K. M. Hock, "Tomographic Reconstruction of the Full 4D Transverse Phase Space," *Nuclear Instruments and Methods in Physics Research A* **726** (2013) 8 – 16.
- [20] P. Spädtke, "The Role of Space Charge Compensation for Ion Beam Extraction and Ion Beam Transport," *Rev. Sci. Instrum.* **85** (2014) 02A744, doi: 10.1063/1.4862661.
- [21] A. W. Chao, M. Tigner, Editors, *Handbook of Accelerator Physics and Engineering*, World Scientific, 1999.
- [22] B. L. Friman, C. Höhne, J. Knoll, S. Leupold, J. Randrup, R. Rapp, P. Senger, editors, *The CBM Physics Book: Compressed Baryonic Matter in Laboratory Experiments* (Lecture Notes in Physics), Berlin: Springer, 2011.
- [23] R. B. Clare, D. Strottman, "Relativistic Hydrodynamics and Heavy Ion Collisions," *Phys. Rep.* **141** (1986) 177 – 280.
- [24] L. P. Csernai, *Introduction to Relativistic Heavy Ion Collisions*, John Wiley & Sons, 1994.
- [25] Yun Cheng, L. P. Csernai, V. K. Magas, B. R. Schlei, and D. Strottman, "Matching Stages of Heavy-Ion Collision Models," *Phys. Rev. C* **81**, 064910 (2010), doi: 10.1103/PhysRevC.81.064910.
- [26] B. R. Schlei, "Extracting the Equation of State of Nuclear Matter through Hydrodynamical Analysis," *Heavy Ion Phys.* **5**, 403 – 415 (1997).
- [27] for more detail, *cf.*, <http://www.wolframalpha.com/input/?i=number+of+atoms+in+the+universe>.
- [28] W. E. Lorenzen and H. E. Cline, "Marching Cubes: A High Resolution 3D Surface Construction Algorithm," *Comput. Graph.* **21** (1987), pp. 163 – 169.
- [29] P. Bourke, "Polygonising a scalar field," May 1994; for more detail, *cf.*, <http://paulbourke.net/geometry/polygonise/>
- [30] B. R. Schlei, "STEVE - Space-Time-Enclosing Volume Extraction Algorithm, Version 1.0," Los Alamos Computer Code LA-CC-04-056, Los Alamos National Laboratory.
- [31] C. Perwass, *Geometric Algebra with Applications in Engineering, Geometry and Computing*, Springer, 2009.